ACS OMEGA

http://pubs.acs.org/journal/acsodf

Article

Experimental Study on Entrainment Characteristics of High-Pressure Methane Free Jet

Yan Lei,* Kai Chang, Tao Qiu,* Xiaofeng Wang, Chao Qin, and Dan Zhou

Cite This: *ACS Omega* 2022, 7, 381−396

Read Online

ACCESS | Metrics & More | Article Recommendations

ABSTRACT: Entrainment occurs during the high-pressure gas jet process, which is crucial for a natural gas direct injection engine. This study presents an experimental investigation on the high-pressure methane jet from one single-hole injector and proposes a method to obtain the entrainment mass flow rate based on kinetic energy conservation. The entrainment is related to three variables, i.e., spring plate moving distance Δx, gas jet mass at the nozzle outlet m_n, and gas jet velocity u_1. A spring-set test rig is built to measure the spring plate moving distance Δx, and the schlieren method is adopted to test the gas jet velocity u_1 based on a constant-volume bomb (CVB) optical test rig; finally, the weight method is used to obtain the methane gas jet mass at the nozzle outlet m_n. This combined measuring method is verified to be valid in the near field to the nozzle. The results show that the methane jet mass flow rate gradually increases along the jet direction and has a two-zone entrainment process. Zone I: near field ($Lr < 10$), the methane jet mass flow rate linearly increases up to the maximum; in the nozzle exit field ($Lr < 1$), it is conserved, and no entrainment occurs. Zone II: far field ($Lr \geq 10$), the jet mass flow rate maintains the maximum, and the entrainment becomes saturated with a saturation value larger than the initial value at the nozzle outlet. The entrainment rate experiences three stages, linearly increasing in stage I and early stage II but not in late stage II and stage III. The methane injection pressure causes great effects on the mass flow rate and entrainment. As the injection pressure increases, the methane jet mass flow rate increases linearly, but the entrainment rate decreases.

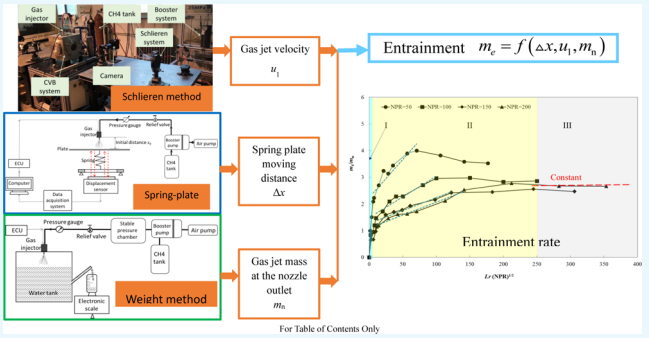

1. INTRODUCTION

As a low-carbon clean gas fuel, natural gas (NG) is an efficient and clean alternative fuel for many power devices[1] and has been widely applied in practical industries such as power plants, vehicle, and marine engines.[2] As for NG applications in internal combustion engines, generally, there are two typical modes for gas fuel supply: one is the direct injection and the other is inlet port injection.[3] For a natural gas direct injection engine, the high-pressure gas fuel directly jets from a tiny nozzle into the engine combustion chamber. Direct injection in cylinder is to inject high-pressure natural gas into the cylinder fluid from a small aperture. Due to the great difference between the NG flow pressure and the environmental air pressure, the natural gas jet has a high speed at the nozzle outlet. The high jet velocity of the natural gas flow induces vortexes due to the great velocity difference between the natural gas jet and the static surrounding air. These vortexes have a direct influence on the energy transfer and air−fuel mixing through their physical processes such as deformation, entrainment, and merging. The NG jet process decides the formation of the combustible mixture and the explosion limits of the air−fuel mixture and finally the ignition and the flame stability.[4] Zhao et al.[5] conducted optical experimental research of high-pressure gas fuel jets, and the results show that the gas concentration distribution is uneven along the axial direction. Hamzeloo et al.[6] used a large-eddy model to investigate the mixing characteristics of hydrogen and methane jets and found that a high nozzle pressure ratio (NPR) causes great effects on the near-nozzle gas jet structure and tip vortices, and they also reported that a higher NPR results in a locally richer mixture. During the gas fuel jet process, the natural gas jet sucks some surrounding air, and this phenomenon is named entrainment. The entrainment of surrounding air results in the spatial evolution of gas jet parameters, such as temperature, velocity, and species concentration distributions, which affects the local air−fuel ratio in the cylinder and determines the accurate fuel control and low emission of the engine.[7,8] Therefore, it is important and necessary to investigate the entrainment

Received: August 31, 2021
Accepted: December 9, 2021
Published: December 29, 2021

characteristics of a high-pressure natural gas jet for optimizing the air−fuel mixing process of natural gas direct injection engines.[9]

The structure of the gas jet under laminar conditions is well characterized. However, as for the high-pressure natural gas jet, it is a turbulent gas flow with a high Reynolds number. The turbulent methane gas jet may experience dilution in a small volume, and the mixture is not uneven but forms a stratification.[10] As the high-pressure natural gas jet continuously penetrates forward along the jet direction, entrainment occurs and enlarges the size of the jet to form a jet cone, but the gas jet velocity and kinetic energy continue to decrease and the mass flow increases. The high-pressure NG has its own characteristics. Sakellarakis et al.[11] conducted both experimental and numerical simulation research studies of high-pressure methane jets, and the results confirmed the hyperbolic decay of axial fuel concentration and the Gaussian shape of traverse concentration profiles in the self-similar region of the jets. Cheng et al.[12] investigated the turbulent plasma jet and reported that the mass flow rate of the ambient air entrained into the turbulent plasma jet is comparatively large and almost directly proportional to the mass flow rate at the jet inlet. Jiang et al.[13] used schlieren to observe the high-pressure natural gas jet characteristics and reported that increasing the NG injection pressure from 3 to 5 MPa enhanced NG jet tip penetration and NG jet volume but decreased the jet cone angle. Moreover, the high-pressure natural gas jet induces shock waves due to its great pressure ratio between the pressure at the nozzle inlet and the surrounding air pressure.[14] Shock waves cause the flow close to the nozzle outlet to be more complex. Cossali et al.[15] studied the entrainment characteristics of an impulsively started gas jet by means of two-dimensional visualizations and laser Doppler velocimetry and found that early in the near field, the jet volume becomes larger and the transient jet entrainment differs significantly from the mechanism responsible for entrainment in the quasi-steady part of the jet. Our previous work[16] revealed that the high-pressure methane jet experiences a dynamic process and that the gas jet after the nozzle outlet is a transient gas jet. Thus, as for the high-pressure transient methane jet, the entrainment has its own characteristics. The entrainment of the high-pressure gas jet is important for the flow patterns in combustion chambers, furnaces, chemical reactors, etc. Therefore, it is important to investigate in detail the law that governs the gas entrainment into a turbulent jet.

Many scholars have carried out a lot of research on the entrainment of a high-pressure gas jet, and the change of mass flow rate in the process of high-pressure gas jet injection is the key content of jet entrainment. It is a useful method to adopt a numerical model to simulate the gas jet flow. Ouellette et al.[17] adopted the multidimensional simulation based on the k-ε turbulence model to evaluate the turbulent transient natural gas injections, and the results showed that the direct injection of natural gas induces the underexpansions of natural gas and the gas fuel flow chokes at the exit of the nozzle, which may have great influences on the entrainment. Wang et al.[18] performed a modeling study to reveal the special features of the entrainment of ambient air into subsonic laminar and turbulent argon plasma jets and found that the presence of the substrate significantly enhances the mass flow rate of the ambient air entrainment. Dong et al.[19] studied the jet development process with different inlet pressures, and the structural evolution of Mach disk pointed out that the high-pressure gas jet pressure leads to the formation of insufficient expansion of gas jet at the nozzle outlet, resulting in a larger near-field angle of jet to promote the spatial distribution and entrainment phenomenon of gas jet; they also calculated the mass flow rate at the nozzle outlet and found that the larger the orifice diameter, the larger is the initial mass flow rate. Deng et al.[20] modeled the high-pressure injection process of hydrogen in argon and nitrogen atmospheres based on the RANS method to study the influence of pressure and shock wave on the entrainment characteristics of hydrogen jet and reported that the jet penetration presents three-stage changes due to the presence of Mach disk, and the entrainment ability of the jet increases with the increase of the nozzle pressure ratio (NPR) at the beginning stage of the jet, but the trend is opposite later. Abraham[21] theoretically deduced a relation for the total mass entrained in a transient gas jet to study the entrainment characteristics of constant-density and variable-density gas jets and found that that the total mass entrained has a cubic dependence on the axial penetration. The above results suggest that the entrainment needs more precise quantitative predictions for practical applications.

There are also many experimental studies to test the entrainment of high-pressure gas jets. Ricou et al.[22] measured the axial mass flow rate (entrainment) in the turbulent jet as the gases (air, propane, carbon dioxide, and hydrogen) jet into a semiclosed chamber by measuring the mass flow rate of the background air entering the jet boundary. Wang et al.[23] directly measured the mass flow rate of the ambient gas entrained into the turbulent plasma jet using the so-called "porous-wall chamber" technique similar to the Ricout method. However, for this method, the gas jet pressure is not too high, and the nozzle diameter is about 0.5 in, which is not suitable for a high-pressure natural gas jet in the DI engine. Furthermore, the introduction of the background air would change the jet boundary and affect the measurement results. Azad et al.[24] used a hot-wire anemometer to measure both the velocity decay rate and entrainment rate of air jets with different nozzle shapes. For the natural gas direct injection engine, the above two methods are not suitable for measuring the mass flow of the high-pressure natural gas jet along the jet axial direction because of its small size, complex flow, instantaneous jet, small cross section in the jet axis direction, and uneven distribution of the mass flow in the cross section. Wang et al.[25] calculated the volume of high-pressure methane jet through schlieren photos on the constant-volume bomb device and obtained the change of air quality sucked by methane jet. However, this method did not consider the incompressibility of a high-pressure methane jet, and during the process of high-pressure methane jet injection, the specific volume is constantly changing.[26] Thus, the entrainment of a high-pressure methane jet cannot be accurately obtained singly based on schlieren images. Tomita et al.[27] applied a path line method utilizing a CCD random shutter camera and a two-component laser Doppler velocity meter (LDV) to observe the jet configuration and the entrainment process and reported that the path line method for estimating the air mass entrainment has good agreement with the values obtained using LDV. Karr et al.[28] and Gilles et al.[29] defined the jet boundary, respectively, using laser-induced fluorescence (LIF) and particle image velocimetry (PIV) technology in the constant-volume vessel to calculate entrainment in gaseous fuel jets. However, the accuracy of the test results is affected by the following feature of the tracer particles, and this method is

https://doi.org/10.1021/acsomega.1c04762
ACS Omega 2022, 7, 381−396

restricted by the LIF and PIV devices. The above literature introduces different methods to measure the entrainment of the gas jet, but the above measurement methods have disadvantages for measuring the entrainment of the high-pressure gas jet. These methods are not suitable for testing the entrainment of the high-pressure methane jet. It is necessary to find an effective test method to accurately obtain the variation in the entrainment of jet mass flow.

For the high-pressure methane gas jet for the NG engine, generally, the nozzle is small (about a tenth of a millimeter to several millimeters), and the gas jet velocity is nearly sonic due to the great pressure difference; thus, it is difficult to utilize a sensor to directly measure the entrainment. Few research studies are reported to effectively measure the entrainment of a high-pressure gas jet. Based on the conservation law of kinetic energy, this paper proposes a new experimental method to measure the entrainment of high-pressure methane gas jet from a tiny single-hole cylindrical nozzle. This work designs the gas jet test rig to examine the high-pressure methane jet and conducts experiments under various operating conditions. The entrainment mass of the methane jet is derived based on the test results based on the kinetic energy conservation.

2. HIGH-PRESSURE GAS JET AND ENTRAINMENT PROCESS

2.1. Gas Free Jet Process. A large number of research results have been obtained on the variation of velocity, kinetic energy, and mass flow of high-pressure gas jet. Figure 1 shows

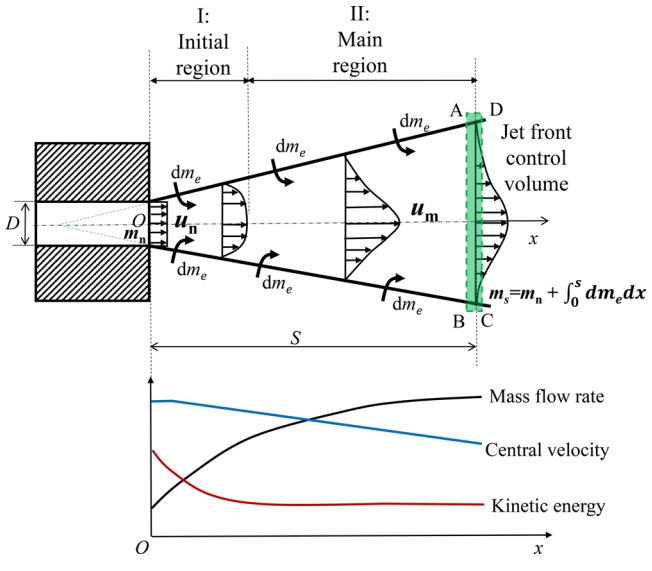

Figure 1. Schematic diagram of a gas jet.

the gas jet process and the jet parameters of a single-hole cylindrical nozzle with a diameter of D. At the nozzle outlet, the gas flow has uniformly distributed properties, such as a mass of m_0 and a velocity of u_0. The x-axis represents the gas jet direction. The zero point O of the x-axis is exactly the center of the nozzle outlet. Here, microcontrol volume ABCD is the front part of the gas jet, and the distance from the zero point O to this control volume in x is defined as S. The initial velocity u_n of the gas jet leaving the nozzle outlet is uniformly distributed. As the gas jet penetrates forward along the x-direction, the axial velocity is the maximum in the central, and it gradually decreases to zero along the radial coordinate. Moreover, with an increase in the x-value of the axial coordinate, the central velocity keeps the initial velocity for a certain time and then decreases gradually. During the gas jet penetration process, the surrounding air is continuously sucked, which makes the boundary of the jet wider, and the mass flow rate increases. Although the mass flow rate increases gradually, it is not enough to offset the decrease of the gas jet velocity, and so the kinetic energy of the gas jet decreases with the increase of x. The changes of the gas jet central velocity, the mass flow rate, and the kinetic energy are shown in Figure 1. The jet region where the center velocity keeps the initial velocity u_n just at the nozzle outlet is called the jet core region, marked as region I. The jet section from the nozzle hole to the end of the core region is called the initial region. In the initial region, the mass flow rate increases continuously. The jet after the initial region is called the main region. Region II locates after region I. In region II, the jet entrainment occurs, and the gas fuel jet and the sucked surrounding air mix together. Thus, region II is called the mixing region. Along the direction of the jet, the entrainment of the surrounding air continuously occurs during the gas jet process. For the microcontrol volume ABCD, the air entrainment mass is dm_e, and the entrainment mass at position S is the sum of the original gas jet mass m_n and the air entrainment along the x-axis, i.e., $m_s = m_n + \int_0^s dm_e\, dx$.

For the high-pressure gas jet, the velocity at the nozzle may reach sonic speeds, and the shock wave tends to appear in the initial section. Therefore, the flow characteristics in this section (near field) are quite complex, which causes great influence on the jet parameters such as the jet mass flow rate and jet kinetic energy. Moreover, the entrainment process and feature of the high-pressure methane jet also have their own characteristics.

2.2. Gas Jet Impact Process. In this work, the high-pressure methane gas directly impacts on a plate-spring test device. This plate-spring is an elastic system that may move together with the methane gas jet by the gas impingement force. When the high-pressure methane gas jet impacts on an elastic body, there is energy transfer between the gas jet and the elastic body. Figure 2 shows the gas turbulent jet impingement process of the control volume ABCD with an elastic plate-spring E. Plate E locates at the position $x_0 = S_0$. The high-pressure gas jets from the nozzle outlet and moves toward plate E. At time t_0, the gas turbulent jet front ABCD almost reaches plate E, and the control volume has a kinetic energy of e_0. Then, very soon after t_0, at time t_1, the control volume comes in contact with plate E; the ABCD has an energy of e_0, while plate E locates at S_1. At the moment the gas jet just meets plate E, the plate E does not move, and thus, $x_0 = x_1 = S_0 = S_1$. After that, at time t_2, the gas jet acts on plate E and pushes it to move to S_2 and the spring is compressed x_2; then, plate E begins to move at a speed of u_2. Plate E moves in a short time (from t_2 to t_3) to compress the spring further, which is the exact gas jet impingement period and has a velocity u_3.

The energy per unit mass of the control volume e can be expressed as

$$e = e_u + gz + \frac{u^2}{2} \tag{1}$$

where e_u is the internal energy per unit mass, g is the gravitational acceleration, z is the height of the central mass of the control volume, and u is the velocity.

https://doi.org/10.1021/acsomega.1c04762
ACS Omega 2022, 7, 381−396

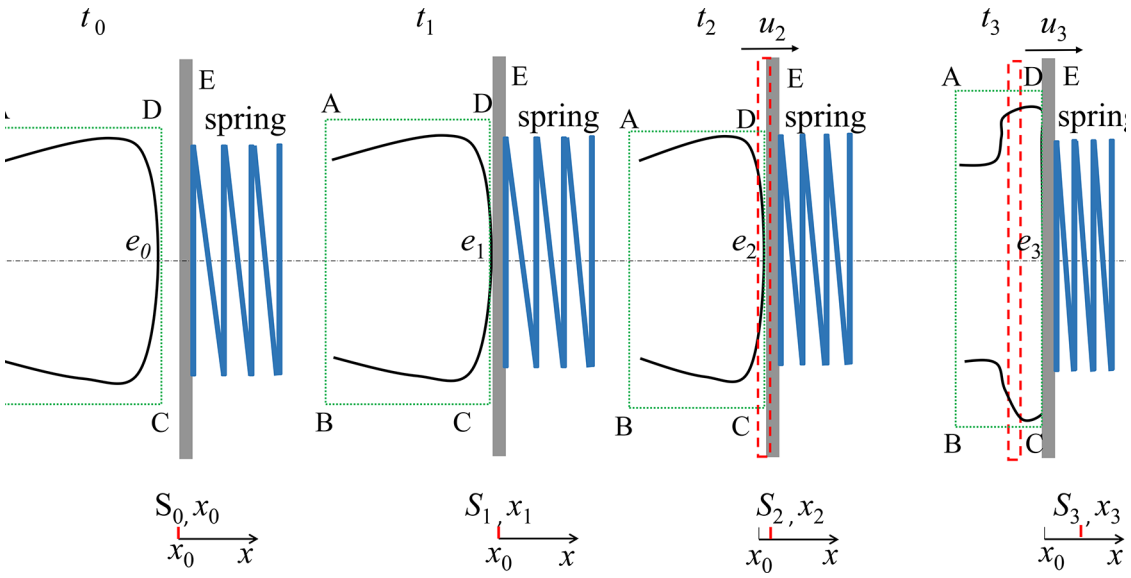

Figure 2. Gas turbulent jet impingement process.

Here, this gas jet impingement model ignores the change of internal energy and the gravity effect, and then the energy of the control volume is just the kinetic energy, i.e.,

$$e = \frac{u^2}{2} \tag{2}$$

Due to the infinite short impingement period (t_1 to t_3), we assume that this process is adiabatic and there is no heat exchange between the control body ABCD and the environment; thus, the energy of the control volume ABCD is conserved during the infinite short impingement period. Equation 3 gives the energy conserved.

$$\frac{1}{2}\rho_1 V_1 u_1^2 - \frac{1}{2}\rho_2 V_2 u_2^2 = w_s \tag{3}$$

where ρ is the density, V is the volume, and w is the work.

For the infinite short impingement process, it is assumed that this gas jet impingement process is a rigid collision, and there is no compression. For this hypothesis, the control volume will spread to the edge along the plate, and it has no deformation to absorb any kinetic energy. Based on the above analysis, the density, volume, and center of gravity may remain the same during the process. According to the energy conservation law, the kinetic energy of the control volume is converted into the energy of the test plate-spring system. It is believed that after the control volume impacts on the test plate, it attaches to the test plate and moves with the plate at the same speed. Thus, the gas jet control volume (with a mass of m_1), the plate (with a mass of m_2), the spring (with a mass of m_3) move forward at the same speed, and the correlations in this movement are as shown in eq 4.

$$\frac{1}{2}m_1 u_1^2 - \frac{1}{2}m_1 u_2^2 = \frac{1}{2}m_2 u_2^2 + \frac{1}{6}m_3 u_2^2 + \frac{1}{2}k\Delta x^2 \tag{4}$$

where k represents the spring elastic potential energy, Δx represents the compression of the spring and is also the displacement of the test plate, and m_1, m_2, and m_3, respectively, represent the mass of the gas jet control volume, the plate, and the spring. The left side of the equation is the gas jet kinetic energy E_{gas}, and the right side is the kinetic energy of the spring plate device E_{spring}.

From eq 4, the gas jet mass m_1 may be derived as follows.

$$m_1 = \frac{\frac{1}{2}m_2 u_2^2 + \frac{1}{6}m_3 u_2^2 + \frac{1}{2}k\Delta x^2}{\frac{1}{2}u_1^2 - \frac{1}{2}u_2^2} = \frac{E_{spring}}{\frac{1}{2}u_1^2 - \frac{1}{2}u_2^2} = \frac{2E_{gas}}{u_1^2 - u_2^2} \tag{5}$$

For a high-pressure methane gas jet, the injection pressure is high and the nozzle diameter is small, and thus, the gas velocity at the nozzle outlet can reach sonic speeds and the Reynolds number is high.[16] When the fluid density is uniform, the Reynolds number is high, and the distance x is much larger than the diameter of the nozzle orifice, the mass flow rate m is proportional to the distance x. More precisely, the jet mass flow rate may be described by the following equation[22]

$$\frac{m_1}{xM^{1/2}\rho_{air}^{1/2}} = K_1 \tag{6}$$

where M stands for the excess momentum flux of the gas jet, ρ_{air} is the density of the surrounding air, and K_1 is a numerical constant. For the methane gas jet, consideration of Newton's second law of motion shows that since the static pressure of the flow is uniform, the jet momentum flux M is conserved, and it is independent of x. Thus, we obtain

$$M = M_{nozzle} = \frac{1}{4}\pi d_{nozzle}^2 \rho_{CH4} u_{CH4}^2 \tag{7}$$

where d_{nozzle} is the nozzle diameter and ρ_{CH4} and u_{CH4} are, respectively, the methane density and velocity just at the nozzle outlet.

We obtain eq 8 based on both eqs 6 and 7.

$$m_1 = K_1 x M^{1/2}\rho_{air}^{1/2} = \frac{\sqrt{\pi\rho_{air}\rho_{CH4}}}{2}K_1 d_{nozzle} u_{CH4} x \tag{8}$$

For a gas jet from a given structure nozzle, the gas injection pressure and the back pressure of the environment air are constant, which means that the jet velocity at the nozzle outlet is also constant. In addition, the surrounding air density is

https://doi.org/10.1021/acsomega.1c04762
ACS Omega 2022, 7, 381−396

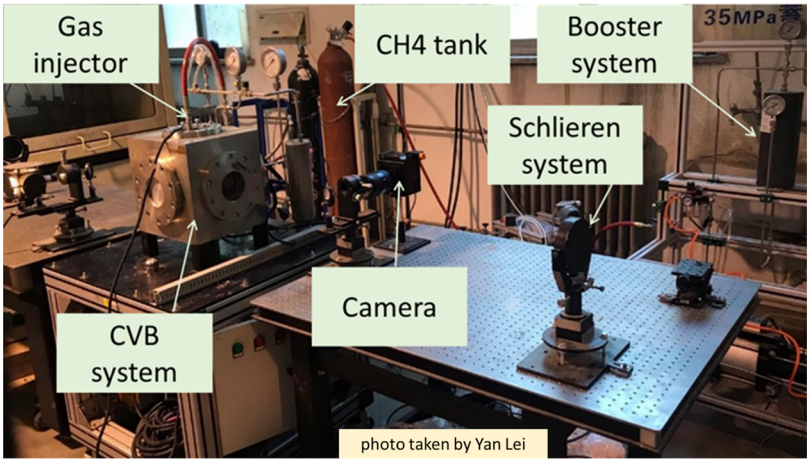

Figure 3. Optical CVB test rig.

constant. Thus, the gas jet mass flow rate is proportional to x, i.e., $m_1 \propto x$.

The gas jet mass at position S m_1 is the sum of the gas jet mass at the nozzle outlet and the entrainment mass m_e, as described in eq 9.

$$m_1 = m_n + m_e = \frac{2E_{gas}}{u_1^2 - u_2^2} \tag{9}$$

Combining both eqs 5 and 9, the entrainment can be derived by eq 10.

$$m_e = m_1 - m_n = \frac{2E_{gas}}{u_1^2 - u_2^2} - m_n = \frac{2E_{spring}}{u_1^2 - u_2^2} - m_n \tag{10}$$

In eq 10, the energy of the spring plate set is described by $\frac{1}{2}m_2u_2^2 + \frac{1}{6}m_3u_2^2 + \frac{1}{2}k\Delta x^2$. Thus, eq 10 is converted to eq 10a, which represents the entrainment.

$$m_e = \frac{2}{u_1^2 - u_2^2}\left(\frac{m_2u_2^2}{2} + \frac{m_3u_2^2}{6} + \frac{kVx^2}{2}\right) - m_n = \frac{2}{u_1^2 - \left(\frac{d\Delta x}{dt}\right)^2}\left[\left(\frac{3m_2 + m_3}{6}\right)\left(\frac{d\Delta x}{dt}\right)^2 + \frac{kVx^2}{2}\right] - m_n \tag{10a}$$

For this test system, once the plate-spring test device is certain, there are several given constants, such as m_2, m_3, and k. In addition, the spring energy is proportional to the spring plate moving distance Δx, which can be tested with a distance sensor, and then the plate speed u_2 is also deduced by derivation of the distance Δx, i.e., $u_2 = \frac{d\Delta x}{dt}$. Thus, in 10a, there are three variables, i.e., the spring plate moving distance Δx, the gas jet mass at the nozzle outlet m_n, and the gas jet velocity u_1, as described in eq 11.

$$m_e = f(Vx, u_1, m_n) \tag{11}$$

According to 10a and 11, the entrainment of gas jet depends on these three parameters, which have practical physical meanings. The spring plate moving distance Δx represents the impingement force or energy of the gas jet at a certain position S along the jet direction, which forces the spring to move. u_1 is exactly the gas jet velocity at a certain position S along the jet direction, which indicates the jet kinetic energy of the gas jet. The gas jet mass at the nozzle outlet m_n is just the source mass of the gas jet, which directly decides the total jet energy. These parameters represent the kinetic energy of both the jet source and the local position along the jet direction, which directly affects the entrainment. Once these three parameters (i.e., Δx, m_n, and u_1) are tested, the air entrainment can be deduced based on the equation. As a result, in this work, we propose an experimental method to test the gas jet velocity and the gas jet mass just at the nozzle outlet.

2.3. Entrainment Rate. Because of entrainment, the methane gas jet mass flow rate m_1 increases and exceeds the initial gas mass flow rate at the nozzle outlet m_n. The ratio m_1/m_n stands for the entrainment capacity of the gas jet. This entrainment rate m_1/m_n may be deduced by assuming that the gas jet is of uniform density. For the methane gas jet at the nozzle outlet, the mass flow rate is defined by the following equation

$$m_n = \frac{1}{4}\pi d_{nozzle}^2 \rho_{CH4} u_{CH4} \tag{12}$$

where d_{nozzle} is the nozzle diameter and ρ_{CH4} and u_{CH4} are, respectively, the methane density and velocity just at the nozzle outlet.

The ratio is deduced by combining eqs 13−15.

$$\frac{m_1}{m_n} = \frac{K_1 x M^{1/2} \rho_{air}^{1/2}}{\frac{1}{4}\pi d_{nozzle}^2 \rho_{CH4} u_{CH4}} = \frac{2K_1}{\sqrt{\pi}}\frac{x}{d_{nozzle}}\sqrt{\frac{\rho_{air}}{\rho_{CH4}}} = \frac{2K_1 Lr}{\sqrt{\pi}}\sqrt{\frac{\rho_{air}}{\rho_{CH4}}} \tag{13}$$

In addition, according to the equation of state of an ideal gas, the density ratio is the proportion of pressure ratio NPR.

$$\frac{m_1}{m_n} = \frac{K_1 x M^{1/2} \rho_{air}^{1/2}}{\frac{1}{4}\pi d_{nozzle}^2 \rho_{CH4} u_{CH4}} = \frac{2K_1}{\sqrt{\pi}}\frac{x}{d_{nozzle}}\sqrt{\frac{\rho_{air}}{\rho_{CH4}}} = \frac{2K_1 Lr}{\sqrt{\pi}}\sqrt{\frac{p_{air}}{p_{CH4}}\frac{R_{CH4}}{R_{air}}} \tag{14}$$

Equation 16 reveals that the entrainment rate m_1/m_n has a relation with the parameters such as Lr and NPR, i.e.,

https://doi.org/10.1021/acsomega.1c04762
ACS Omega 2022, 7, 381−396

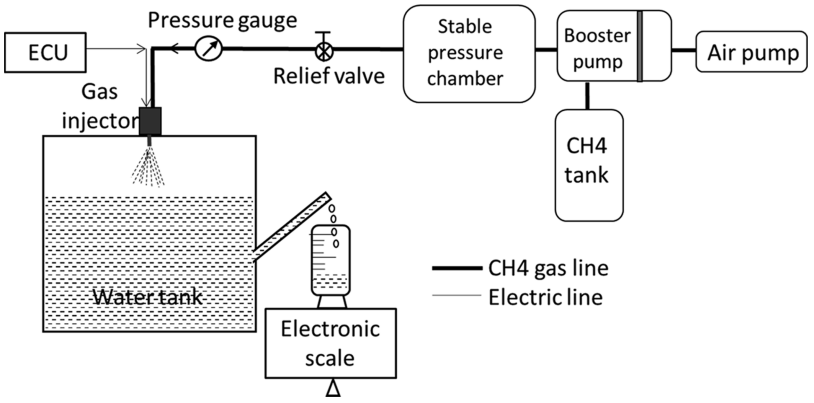

Figure 4. Gas jet at the nozzle outlet test rig.

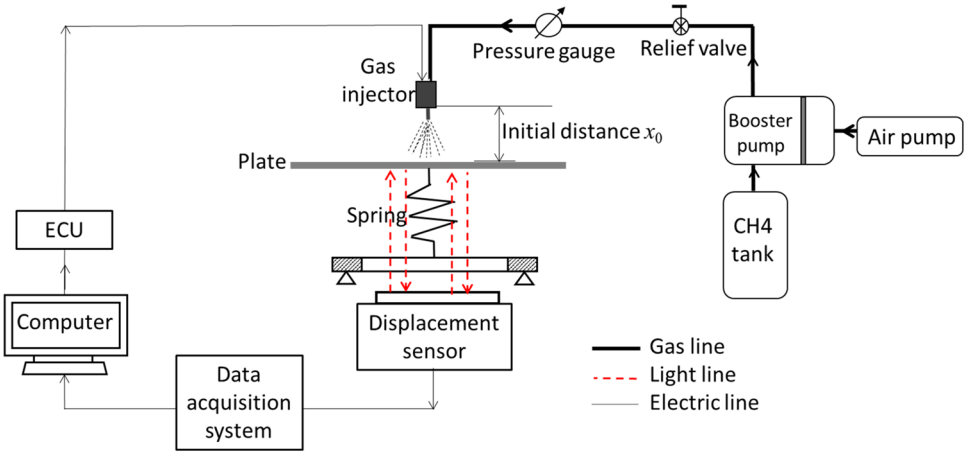

Figure 5. Test rig for the kinetic energy of methane gas jet.

$$\frac{m_1}{m_n} \propto Lr\sqrt{\mathrm{NPR}} \tag{15}$$

3. EXPERIMENTAL RESEARCH

As stated in the analysis in Section 2, it is necessary to test the two important parameters of the gas jet, one is the gas jet velocity and the other is gas jet mass at the nozzle outlet. In this work, we first build an optical test rig based on a constant-volume bomb (CVB) system to visually observe the gas jet process and test the gas jet penetration distance. The gas jet velocity of the gas jet front is just the derivation of the gas penetration. Moreover, we also design the test device to detect the high-pressure gas injector features such as the jet mass flow rate. Finally, we build a plate-spring test rig to measure the gas jet impingement kinetic energy. According to all of the above experimental results, based on eqs 10a and 11, the entrainment can be deduced.

3.1. Optical Test of Methane Gas Jet Penetration. To meter the gas jet velocity u_1, this work adopts the schlieren method to test the methane gas penetrate velocity. An optical constant-volume bomb (CVB) test rig, as shown in Figure 3, is designed to observe the high-pressure gas turbulent jet under the condition of varied injection pressure $p_{\mathrm{injection}}$ and back pressure p_b. The CVB system, made of steel, is a cuboid with an inner cylindrical bore with a total volume of 13 L. The size of the CVB cuboid is length × width × height = 330 mm × 300 mm × 300 mm. A high-pressure single-hole injector with a diameter of 1 mm locates on the top center of the CVB. During the experiments, the CVB cylinder is first filled with air of back pressure p_b from an air tank, and the high-pressure air jet test begins after a 5 min standing of the total CVB test rig. A series of optical test devices including a schlieren system and a high-speed camera are used to observe the high-pressure methane gas injection process. The methane gas injection timing is triggered by an electronic control unit (ECU) developed by the authors and set to be synchronous with the camera. More details of the CVB test rig and the postprocessing method of the optical test images are illustrated in the authors' published literature[16] in detail. The injection pressure $p_{\mathrm{injection}}$ is adjusted ranging from 0.1 to 30 MPa, while the back pressure p_b is controlled ranging from 0.1 to 5 MPa.

3.2. Test of Methane Gas Jet at the Nozzle Outlet. To meter the gas jet mass at the nozzle outlet m_n, this work uses the weight method to measure the methane gas jet mass of the single-hole gas injector. Figure 4 shows the gas injection mass test schematic diagram. The high-pressure gas injector is mounted on the top of a water tank. There is a small pipe extending from the lower part of the water tank, and the water is adjusted to be just at the outlet of the pipe without any drop out. The upper part of the water tank is full of air sealed between the tank head and water. As the high-pressure methane gas jets into the sealed space, these gases can push water to move out of the pipe, and the discharged water from the pipe is collected by the metering cylinder.

For this test, the methane gas jet mass is deduced based on the discharged water mass. According to this test method, the

https://doi.org/10.1021/acsomega.1c04762
ACS Omega 2022, 7, 381−396

methane gas injection volume V_{CH4} is equal to the discharge water volume V_{water}, as shown in eq 16.

$$V_{CH4} = V_{water} = \frac{m_{water}}{\rho_{water}} \tag{16}$$

where m_{water} is the water mass and ρ_{water} is the water density. The density of the methane ρ_{CH4} changes as the hydrogen gas pressure p_{CH4} varies. The relationship between the air density and the air pressure is defined by the gas state equation (eq 17).

$$\rho_{CH4} = \frac{p_{CH4}}{zRT_{CH4}} = \frac{p_{in}}{zRT_0} \tag{17}$$

where T_{CH4} is the methane temperature (here, equal to the environmental temperature T_0), R is the conventional gas constant, and z is the real gas compression coefficient. Both R and z are constants.

The methane injection mass m_n is defined by eq 18.

$$m_n = \rho_{CH4} V_{CH4} \tag{18}$$

Thus, the gas jet mass at the nozzle outlet m_n is derived.

3.3. Testing of Gas Jet Kinetic Energy. To measure the kinetic energy of methane gas jet, a plate-spring elastic test system is designed, as shown in Figure 5. The gas jet kinetic energy test system mainly contains four parts: the high-pressure gas supply system, the measuring device, the electronic injection unit, and the data acquisition system. The high-pressure booster pump supplies the gas injector with high-pressure methane for gas jet testing. The injection pressure of the gas injector is able to be adjusted. In addition, the electronically controlled injection unit ECU regulates the injection timing. The high-pressure methane directly impacts on a plate-displacement device.

This plate-spring system is important for this test. First, to support the gas impact, it should be light enough to easily move as the gas jet impacts on it even if the gas jet has a small impact energy. In this test, the plate is plastic and it is light with a weight of 0.253 kg. In addition, to ensure the gas jet is totally impacting on the plate, the plate should be large enough. This plate has a larger diameter of 80 mm, 80 times the injector nozzle, which has a far larger area than the gas jet cover area to receive almost all of the jet gas. Moreover, the spring is designed to have suitable stiffness, not too hard or soft. Here, the spring is designed to have a stiffness of 5038.2 N/m. The spring seat is fixed, and it adheres to the testing plate. Thus, both the plate and the spring form an elastic device located in the vertical direction of the methane gas jet, and the plate is set to be located at different initial positions along the jet direction, i.e., with varied initial distances x_0.

As the gas jets and directly impacts on the plate, the elastic plate-spring set moves together at the same speed by the force of the high-pressure methane gas jet. The optical displacement sensor records the movement of the plate. For each test condition, the test repeats three times, and the average value is taken to ensure the accuracy of the test results. All of the data are transferred to the computer for further postprocessing by the data acquisition system.

The test apparatus for the optical test of methane gas jet penetration is illustrated in our previously published literature.[16] Those test devices used in tests of both the gas jet at the nozzle outlet and the gas jet kinetic energy are described in Table 1. For each kind of experiment, the gas jet is tested under varied operating conditions. Table 2 presents the details of the gas injector and the gas jet operation conditions.

Table 1. Test Apparatus

type		specification	
displacement sensor	μ-ε optoNCDT 1700-50	range	0−50 mm
		sensitivity	0.001 mm
		operating temperature	0−50 °C
pressure gauge	R04.4311	range	0−40 MPa
		accuracy	1% full scale
		operating temperature	−40 to 60 °C
electronic scale	RMPUT	range	0.0005−7.5 kg
		accuracy	0.0001 kg
		operating voltage	220 V
data acquisition unit	Dewe-43	acquisition frequency	100 kHz
air pump	W0.9/8	rated outlet pressure	0.8 MPa
		rated rotation	930 r/min
		volume flow	0.9 m^3/min
gas booster pump	OLF-2530	rated outlet pressure	0.7 MPa
		rated rotation	1400 r/min
		volume flow	165 L/min
		boost ratio	60:1
		gas inlet pressure	0.01∼1 MPa
		driving gas pressure	≤0.8 MPa

Table 2. Test Device Specifications and Operating Conditions

type		specification
test device	injector	single-hole nozzle, nozzle diameter: d_{nozzle} = 1 mm
	plate	diameter: 80 mm, mass: m_2 = 0.253 kg
	spring	stiffness: k = 5038.2 N/m, mass: m_3 = 0.373 kg
test condition	test gas	air
	environment temperature	288 K
	injection pressure	5 MPa, 10 MPa, 15 MPa, 20 MPa, 25 MPa
	ambient pressure	0.1 MPa
	injection time pulse	18 ms
	plate initial position S	0.2 mm, 0.5 mm, 0.8 mm, 1 mm, 1.5 mm, 2 mm, 3 mm, 4 mm, 5 mm, 8 mm, 10 mm, 12 mm, 15 mm, 20 mm, 25 mm

4. RESULTS AND DISCUSSION

To illustrate the gas jet performance, here two nondimensional parameters are introduced. The relative position Lr is the ratio between the initial position of the test plate x_0 to the injector nozzle diameter d_{nozzle}, i.e., $Lr = x_0/d_{nozzle}$. The nozzle pressure ratio NPR is the gas injection pressure $p_{injection}$ to the ambient pressure p_b, i.e., NPR = $p_{injection}/p_b$.

The gas injector begins to release the high-pressure gas and finally stops the injection by ECU controlling signals. The injection pulse is a key parameter for the injection control, and it affects the injection duration. This work conducts experi-

https://doi.org/10.1021/acsomega.1c04762
ACS Omega 2022, 7, 381−396

ments under the condition of varied injection pulse. Figure 6 shows the plate displacement under conditions of a constant-

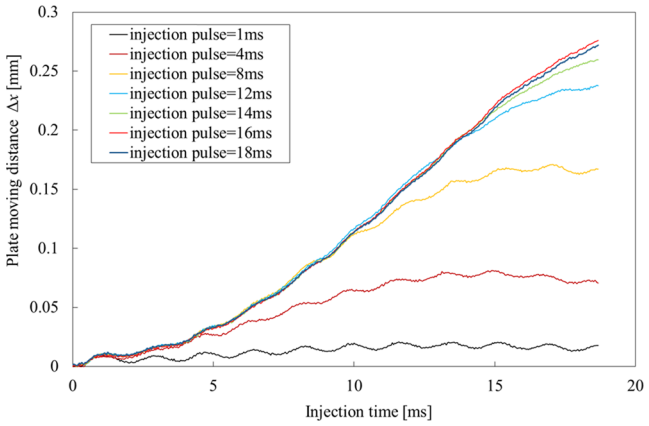

Figure 6. Effect of injection pulse.

pressure ratio (NPR = 150) while injection pulse varies. When the injection pulse increases, the plate moving distance Δx increases. As the injection pulse is small, the differences of Δx among different injection pulse are great, and there are fluctuations. However, as the injection pulse is above 8 ms, the differences of Δx become smaller, and these curves tend to be stable. Once the injection pulse increases up to 18 ms, these curves of the moving distance Δx almost coincide with each other, which means that the injection pulse has little influence on the plate moving distance Δx. Thus, in this work, the injection pulse is set to 14 ms for all of the experiments.

Figure 7 shows the methane gas jet penetration results of the CVB optical test. Figure 7a shows the images of methane jet based on the image process program described in the literature[16] and the methane gas jet tip penetration distance S can be gained. Based on the tip penetration S, the methane jet velocity u_1 is deduced, as shown in Figure 7b, under the condition of different NPRs.

It shows that the methane gas jet velocity rapidly decreases as the gas jets from the nozzle outlet ($Lr = 0$), and it tends to be constant as $Lr \geq 10$. This reveals that the methane gas jet has a two-stage feature. The gas jet penetration velocity curve demonstrates both the deceleration in stage I and relatively constant velocity in stage II. During stage I, the gas penetration velocity decreases sharply, which means that this is an unstable stage due to the varying gas penetration velocity. During stage II, the gas penetration velocity tends to be constant so that it is a stable stage. Furthermore, the gas jet velocity increases with the increase in the NPR.

The methane gas jet kinetic energy performance can be metered based on the spring plate moving distance Δx tested using a distance sensor. Here, we present one example (i.e., NPR = 150, $Lr = 10$) of the investigation results.

Figure 8 shows the plate moving distance Δx under the condition of NPR = 150 and $Lr = 10$. It reveals that the plate moving process is divided into three stages.

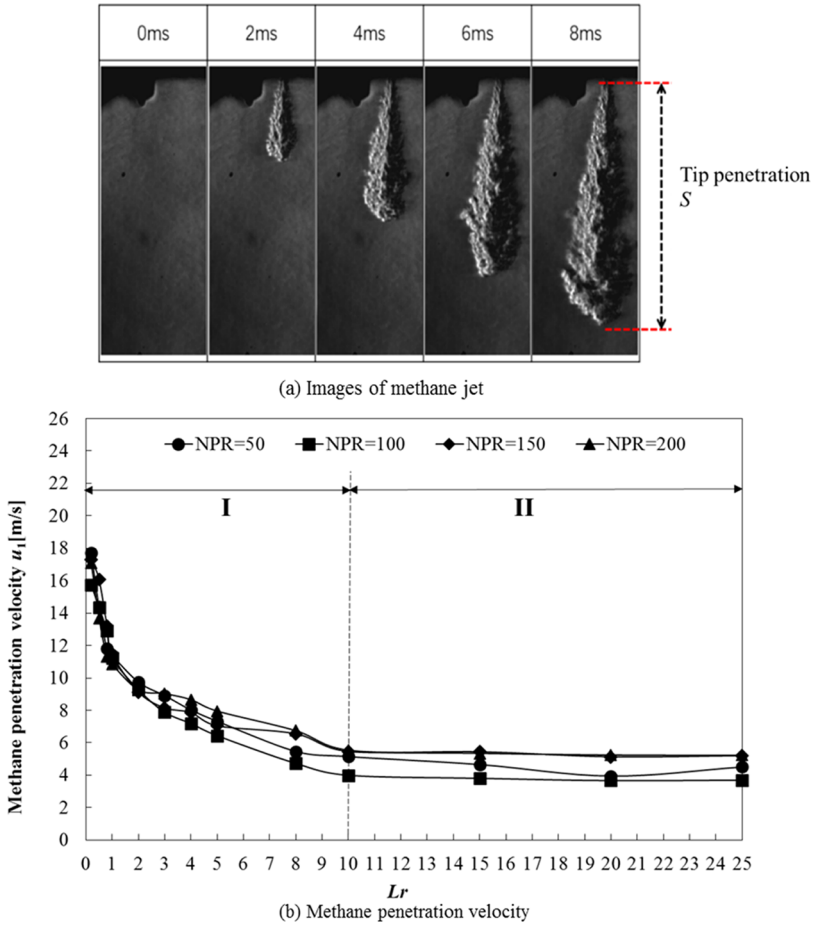

Figure 7. Methane jet penetration characteristics.

https://doi.org/10.1021/acsomega.1c04762
ACS Omega 2022, 7, 381−396

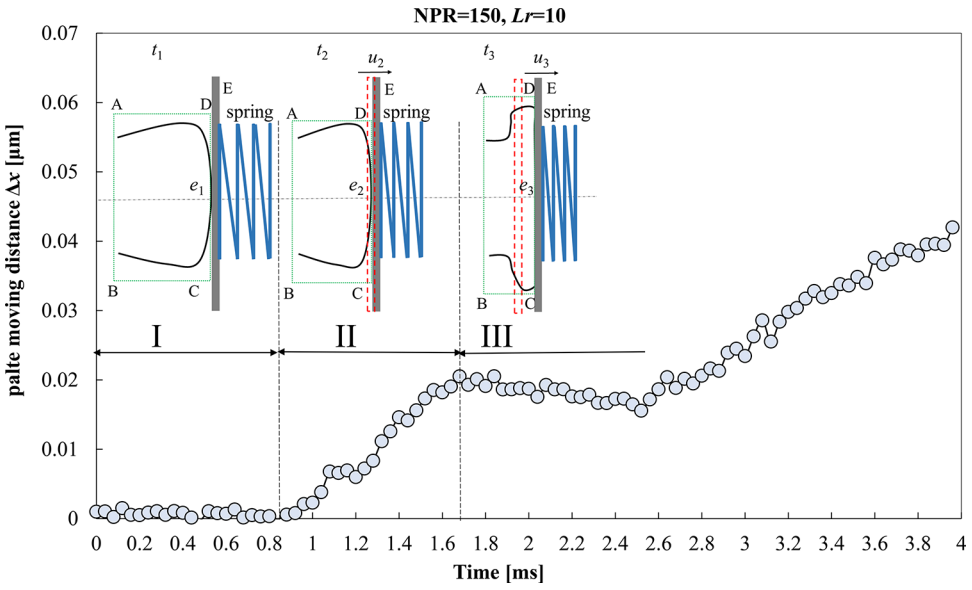

Figure 8. Spring plate moving distance of methane gas jet test.

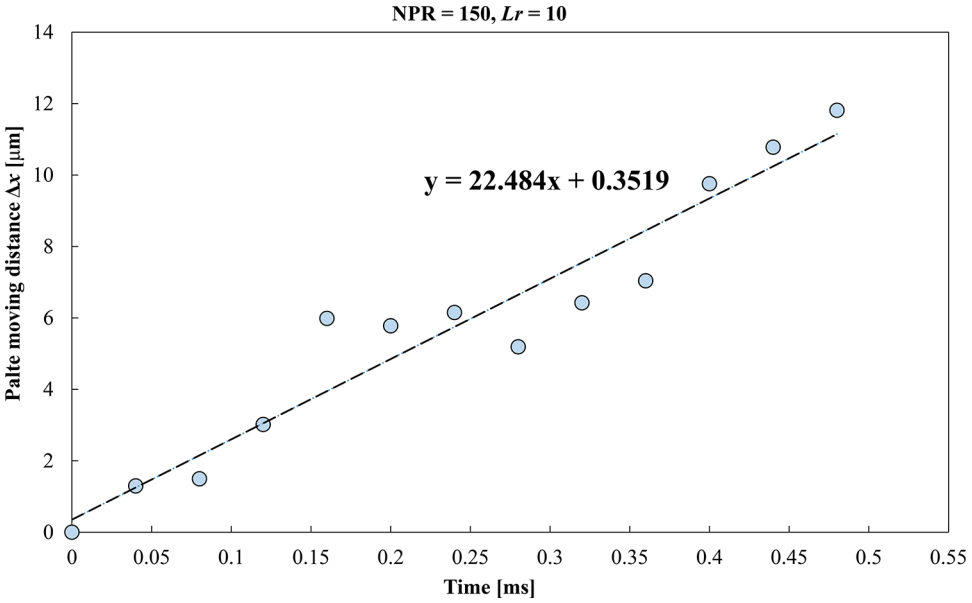

Figure 9. Linear movement of stage II.

Stage I, the idle stage: During the first stage, the plate moving distance Δx is almost zero, and thus, the plate remains stable without any movement. This stage is the first t_1 when the methane gas jet exactly impacts on the plate, as described in Figure 2.

Stage II, the rising stage: After stage I, the plate moving distance Δx begins to increase, and the increasing tendency is nearly linear. This stage is the time t_2 in Figure 2 when the plate begins to move by the action of the methane gas impingement.

Stage III, the fluctuation stage: After stage II, the plate moving distance Δx continues increasing, but this curve has a fluctuation feature; this process is stage III (time t_3). During stage III, the methane gas jet impacts on the plate to push it forward. On the contrary, the methane gas jet begins to be compressed, and the shape of the methane gas jet front changes. Thus, not all of the kinetic energies of the gas jet transfer directly to the plate-spring system to push it forward during stage III due to the gas compression.

According to the above analysis, it shows that the gas jet impact process in stage III is quite different from stages II and I, and it has a fluctuation behavior. The monotone increasing behavior in stage II conforms to the energy conservation law. As a result, the kinetic energy conservation equations (eqs 3 and 9) are valid only during stage I and stage II but not stage III. Therefore, the data in stage II should get more attention.

We focus on the monotone increasing behavior of stage II. Figure 9 shows the details of the plate moving distance Δx during stage II in Figure 8. It reveals this linear movement of the spring plate caused by the high-pressure methane gas jet, and it also gives the linear fitting formula of this movement. Thus, the slope of the linear displacement curve is exactly the plate moving speed u_2 since the definition of the speed is the

https://doi.org/10.1021/acsomega.1c04762
ACS Omega 2022, 7, 381−396

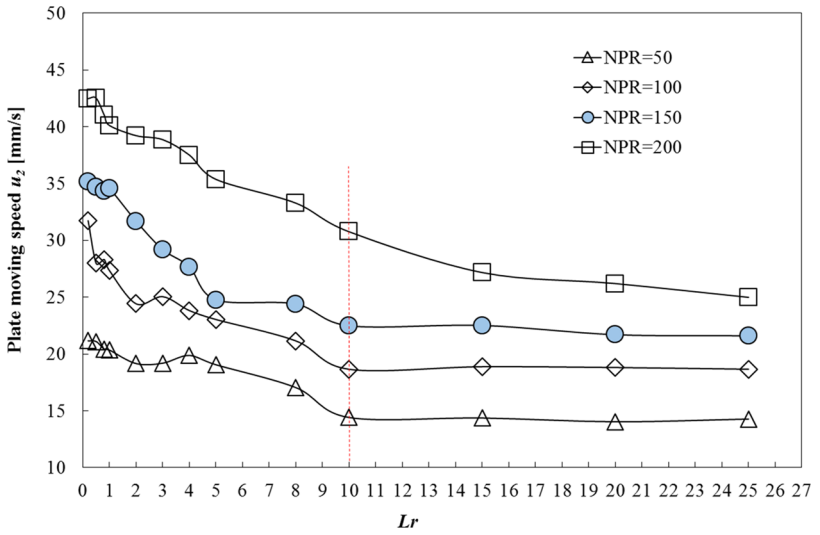

Figure 10. Spring plate moving speed u_2 along the jet direction after the nozzle.

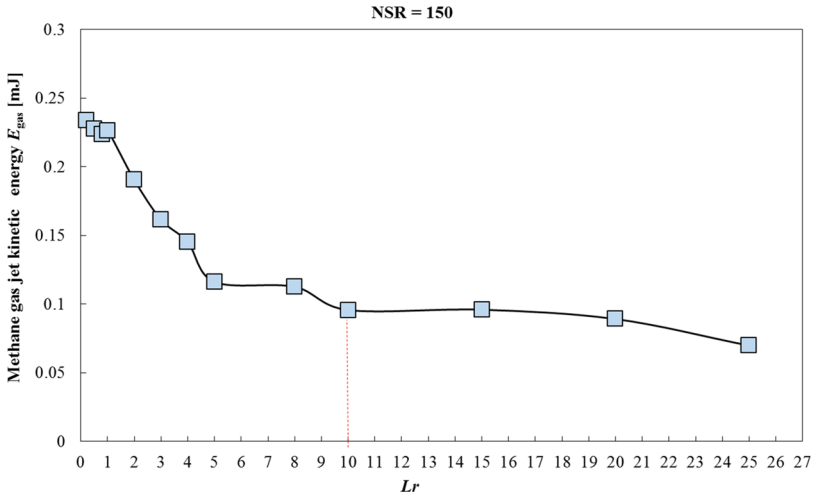

Figure 11. Methane jet kinetic energy E_{gas} along the jet direction.

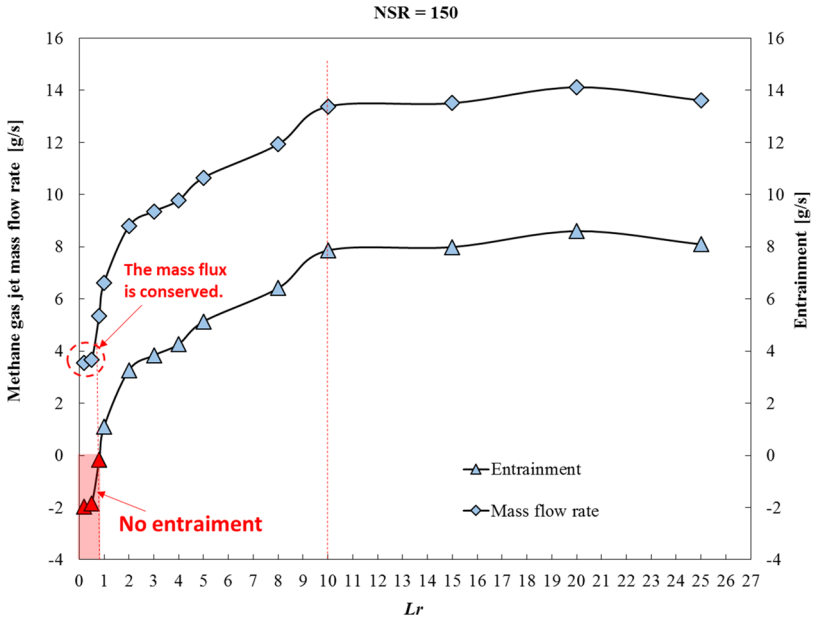

Figure 12. Methane jet mass flow rate and entrainment.

https://doi.org/10.1021/acsomega.1c04762
ACS Omega 2022, 7, 381−396

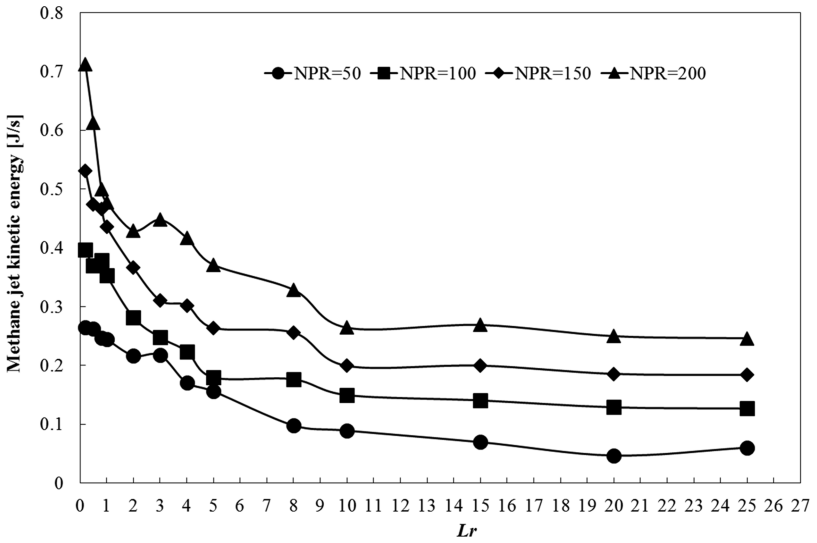

Figure 13. Methane gas jet kinetic energy along the jet direction.

derivation of the displacement. For this operating condition, we obtain u_2 = 22.484 mm/s.

Similarly, the plate moving speed u_2 under varied conditions may be deduced by the experimental results of the plate moving displacement. For each methane gas jet pressure (or NPR), we test the spring plate displacement under the condition of different initial positions of the test plate x_0 (or Lr). Thus, the corresponding plate moving speed u_2 may be obtained. Figure 10 shows the plate moving speed u_2 against Lr under the condition of different NPRs. The results show that the plate moving speed u_2 has a downward trend as soon as the methane jets out of the injector. Moreover, it declines more for a small Lr than for a large Lr. It sharply decreases as $Lr < 10$, which is the field close to the nozzle, and tends to slowly change after $Lr > 10$ (far field to the nozzle), which means a two-stage behavior of the plate moving speed u_2. In addition, for different NPRs, this two-stage behavior occurs.

As the plate moving speed u_2 and the plate moving distance Δx are acquired, the kinetic energy of the spring plate device E_{spring} (i.e., $E_{spring} = \frac{1}{2}m_2u_2^2 + \frac{1}{6}m_3u_2^2 + \frac{1}{2}k\Delta x^2$) can be deduced. The given constants such as the plate mass m_2, the spring mass m_3, and the spring stiffness k are listed in Table 2. Thus, the kinetic energy of the spring plate device E_{spring} may be deduced based on these data. In addition, the kinetic energy of the total system during stage II is conserved. Thus, the kinetic energy of the gas jet E_{gas} is equal to the kinetic energy of the plate-spring device E_{spring}, i.e., $E_{gas} = E_{spring}$.

Figure 11 presents the kinetic energy of the gas jet E_{gas} under the condition of different Lr values while NPR = 150. The results show that the gas jet kinetic energy decreases as soon as the methane jets out of the injector. It sharply declines as $Lr < 10$, which is the field close to the nozzle, and tends to slowly change after $Lr > 10$ (far field to the nozzle). In addition, this methane gas jet kinetic energy E_{gas} has a similar developing tendency as the spring plate moving speed u_2.

Once the gas jet kinetic energy E_{gas}, the methane gas jet velocity u_1, and the spring plate moving speed u_2 have been gained, the mass of the methane gas jet flow m_1 may be deduced based on eq 5. In addition, the entrainment can be deduced based on eq 10 after both m_1 and m_n (i.e., the mass at the nozzle outlet deduced according to the test method in Section 3.2) are derived.

Figure 12 shows the methane gas jet mass flow rate and the entrainment along the jet direction under the condition of different Lr values while NPR=150. Thus, the entrainment of the methane gas jet along the jet direction may be deduced based on this method. Figure 12 reveals the fact that both the methane gas jet mass flow rate and the entrainment have a totally upward trend. Both first rapidly increase, especially in the field close to the nozzle ($Lr < 10$), while both remain stable in the far field ($Lr \geq 10$), which also indicates a two-stage behavior. The turning points (i.e., Lr = 10 marked by a red dashed line) of these two stages for both the methane gas jet mass flow rate and the entrainment coincide with that of the plate moving speed in Figure 10. This increase of the mass flow rate is induced by the gas jet entrainment. The methane gas jet velocity decreases along the jet direction, and most of the energy is transferred to the surrounding fluid. The more the methane gas jet velocity decreases, the more surrounding fluid is sucked into the jet under the suction of the longitudinal vortex, which means entrainment occurs. This entrainment causes an increase in the gas jet mass. In addition, at the very beginning of the jet, the area very close to the nozzle outlet, i.e., $Lr < 1$, marked in the red area, the entrainment tends to be negative. This red nozzle near field is a no-entrainment zone. This no-entrainment phenomenon may be caused by the shock waves due to the high-pressure methane gas jet from a tiny nozzle. Our previous work[16] demonstrates that the high-pressure methane jet reaches its sonic speed at the nozzle outlet and induces shock waves. This shock wave structure enclosed a supersonic gas flow region wherein it is assumed that no entrainment occurs.[30] As there is no entrainment in this zone, the mass flux at the nozzle exit is conserved throughout this region. This no-entrainment phenomenon demonstrates that the total jet mass flow is almost constant in the no-entrainment zone marked by a red dashed circle in Figure 12.

Similarly, the methane gas jet performance under the condition of varied pressure ratios NPR are acquired, and Figure 13 shows the methane gas jet kinetic energy E_{gas} per unit time for different NPRs. It shows that all of the methane gas jet kinetic energy curves tend to decline with the increase

https://doi.org/10.1021/acsomega.1c04762
ACS Omega 2022, 7, 381−396

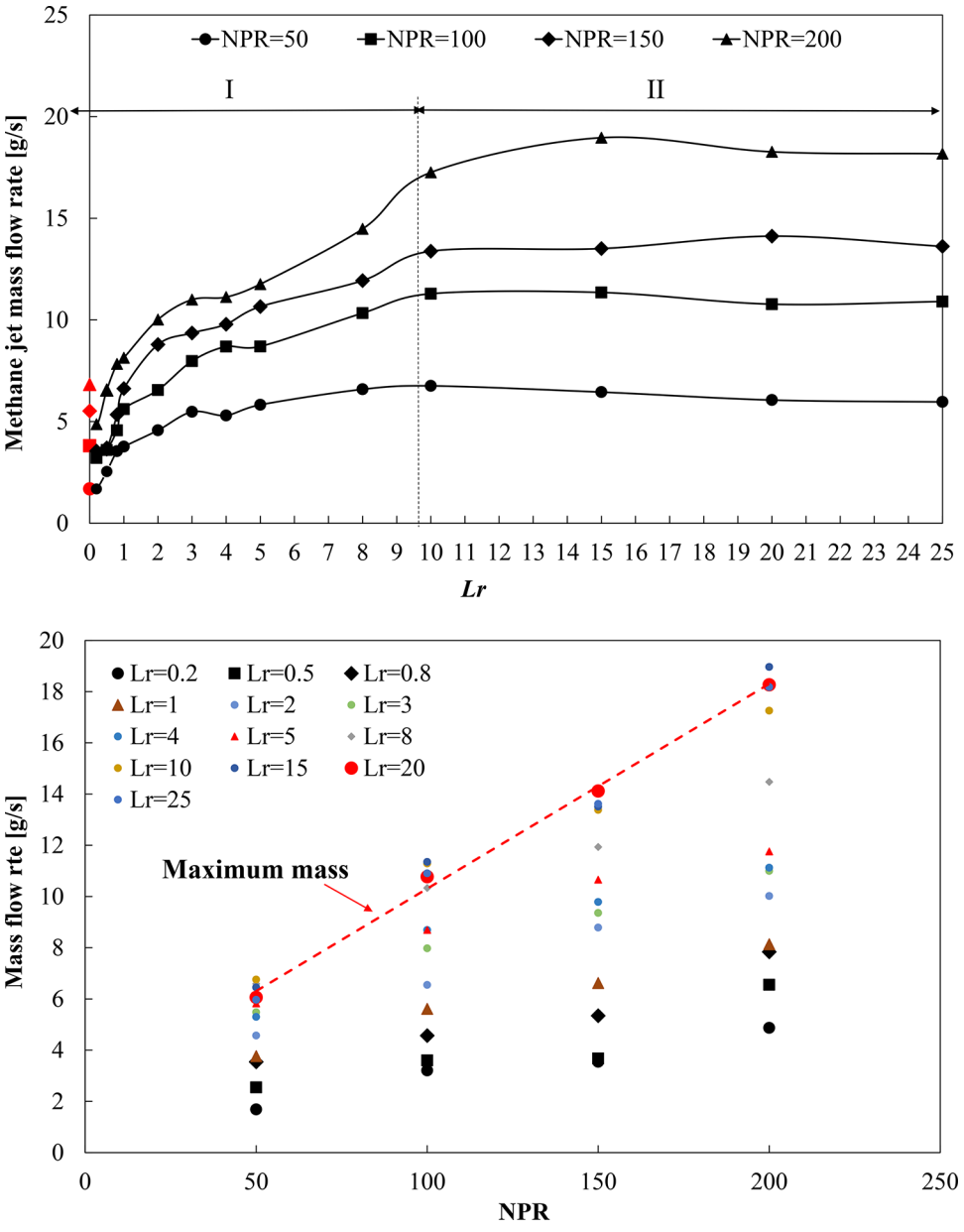

Figure 14. Methane gas jet mass flow rate.

in *Lr*. In addition, they have a greater decline slope as $Lr < 10$ (near field) and become almost stable as $Lr > 10$ (far field). Moreover, the higher the jet pressure (great NPR), the greater the gas jet kinetic energy.

Figure 14 shows the results of the methane gas jet mass flow rate. Figure 14a is the jet mass flow rate along the jet direction under the condition of varied NPRs. These curves have a general upward trend along the jet direction. At the nozzle outlet, i.e., $Lr = 0$, the methane gas flow rate is derived by the experiments described in Section 3.2, and the results at the nozzle outlet are marked in red. The methane gas jet mass flow rate gradually increases along the jet direction. Moreover, it reveals that the methane gas jet mass flow rate has a two-zone feature. In zone I, $Lr < 10$ (near field), the methane jet mass flow rate curves sharply rise and then reach the maximum as *Lr* increases. In zone II, $Lr \geq 10$ (far field), the curves remain constant at the maximum. The mass flow rate reaches its maximum and becomes stable in zone II, and the value is larger than the initial methane jet mass flow rate (red one). This increasing gas jet mass flow rate is due to the entrainment of the gas jet along the jet direction. The surrounding air is drawn inward toward the gas jet, and the total gas mass flow rate increases. Moreover, the entrainment ability of the gas jet tends to reach saturation in zone II. Figure 14b reveals that the jet mass flow rate increases linearly with the increase in NPR (injection pressure). The difference between the maximum mass flow rate and the initial one becomes larger as the NPR (jet pressure) increases. The average maximum mass flow rate is marked by the red dotted line, which is exactly the mass flow rate saturation line. Furthermore, the results also reveal that in zone I, the mass flow rate continues increasing, which means that entrainment occurs; however, it becomes stable in zone II, which means the gas jet does not suck the air anymore, i.e., the entrainment is saturated. Therefore, the characteristics in zone I are more important for the entrainment since most entrainment occurs in this zone.

https://doi.org/10.1021/acsomega.1c04762
ACS Omega 2022, 7, 381−396

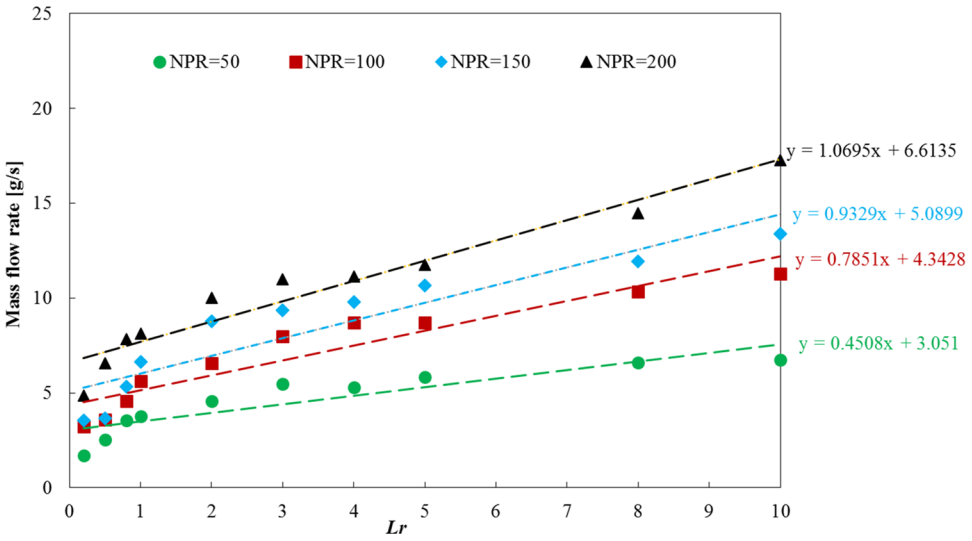

Figure 15. Linear relationship between mass flow rate and *Lr*.

As shown in the curves in Figure 14, in zone I, the mass flow rate has a linear relation to *Lr*. Figure 15 shows the fitting curves of the test data as $Lr \leq 10$. It shows that the fitting curve is linear. The methane gas jet mass flow rate increases linearly with the increase in *Lr* in zone I. As the injection pressure (or NPR) increases, the slope of the fitting line becomes larger. It is worth noting that the interception points of the lines and the vertical axis are exactly the mass flow rate of $Lr = 0$, i.e., the mass flow rate at the nozzle outlet.

Figure 16 shows the comparison between the intercepts of the fitting lines and the test results. It shows that the fitting

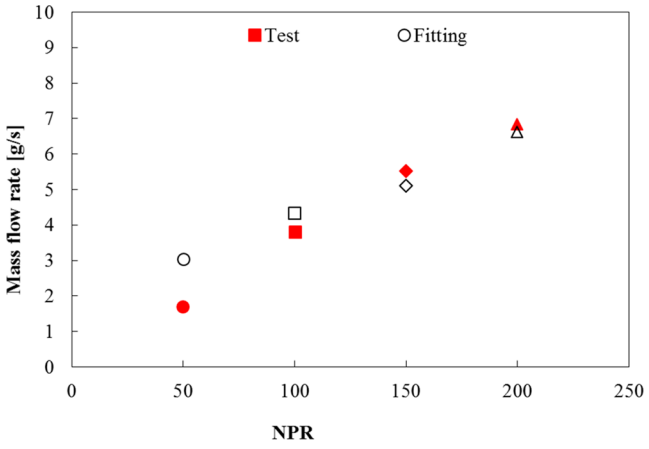

Figure 16. Comparison between fitting value and test result.

values are close to the test values, especially for the high pressure (NPR). Therefore, it also demonstrates the accuracy of deduced gas jet mass flow rate based on the kinetic energy method.

Figure 17 presents the relationship between the entrainment rate and *Lr* $(\mathrm{NPR})^{1/2}$. It shows that the m_1/m_n curves are not linear for all conditions. The m_1/m_n curves experience three stages. The curves coincide with each other at the very beginning (stage I), and then they rise and develop (stage II); however, finally, all curves tend to coincide again to a constant and become stable (stage III). During stage III, all curves tend to coincide with each other to become a constant, and m_1/m_n is then dependent on *Lr* $(\mathrm{NPR})^{1/2}$ without a linear feature anymore. Figure 17 reveals that the m_1/m_n curves have a linear feature in stage I and early stage II but not in late stage II and stage III. This is because the linear relation of eq 17 is deduced based on assuming that the gas jet density is uniform. For the gas jet with a small *Lr* (close to the nozzle outlet), the gas jet has relatively great jet energy and jet velocity to maintain the uniform density in the gas jet cover area. As the gas jet penetrates forward along the jet direction with a large *Lr* (far to the nozzle), the gas jet energy and jet velocity decay due to the surrounding air resistance. In addition, the gas jet draws the surrounding air into the gas jet. Thus, the density of the jet cannot be uniform then.

Stage I is very small and occurs just at the near field very close to the nozzle outlet. During stage I, these curves are linear and almost vertical with a high slope, which indicates a high entrainment velocity. During stage II, the methane gas jet has different entrainment capacities under the condition of varied NPRs (injection pressure). It should be noted that m_1/m_n shows a linear feature against *Lr* $(\mathrm{NPR})^{1/2}$, which demonstrates the relation in eq 17. Moreover, the entrainment rate is higher for a lower NPR, and it has a greater slope, as shown in Figure 18.

In Figure 18, the horizon abscissa is the NPR (represents the injection pressure), and the vertical one is the slope of the m_1/m_n curve in Figure 17, i.e., $\frac{\mathrm{d}\left(\frac{m_1}{m_n}\right)}{\mathrm{d}(Lr\sqrt{\mathrm{NPR}})}$. The gas jet entrainment capacity tends to decrease as the NPR increases. Once the NPR increases sufficiently high, the curves tend to be close together with the same slope. Therefore, for a given nozzle size, it is not useful for increasing gas jet entrainment capacity only by increasing the gas jet pressure.

5. CONCLUSIONS

This paper presents an experimental method to measure the entrainment mass of a gas jet according to the principle of kinetic energy conservation. The entrainment of methane gas jet is related to three variables, i.e., spring plate moving distance Δx, gas jet mass at the nozzle outlet m_n, and gas jet velocity u_1. This measuring method is verified to be valid in the near field to the nozzle.

https://doi.org/10.1021/acsomega.1c04762
ACS Omega 2022, 7, 381−396

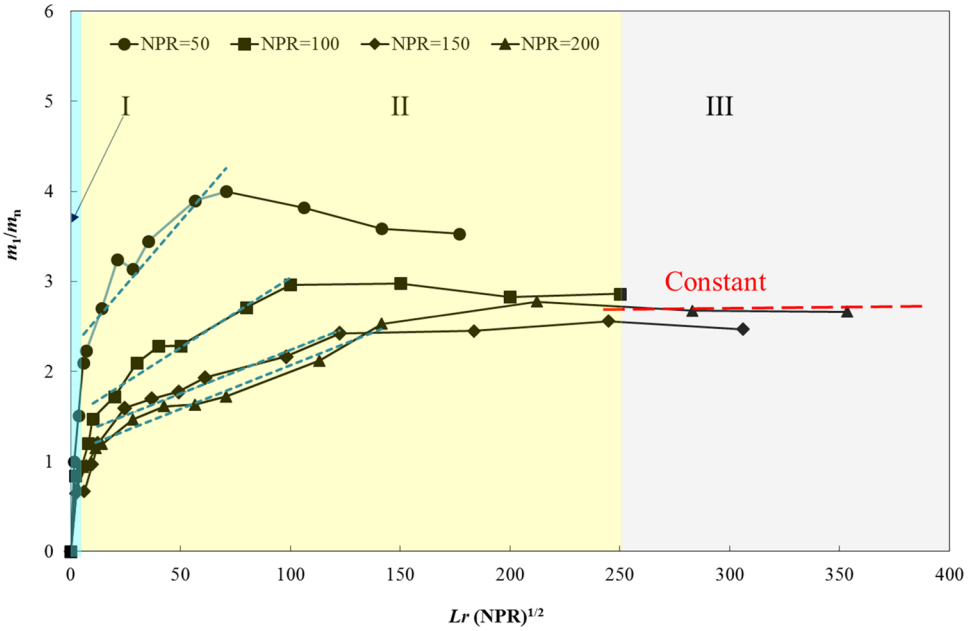

Figure 17. Entrainment rate for methane jet.

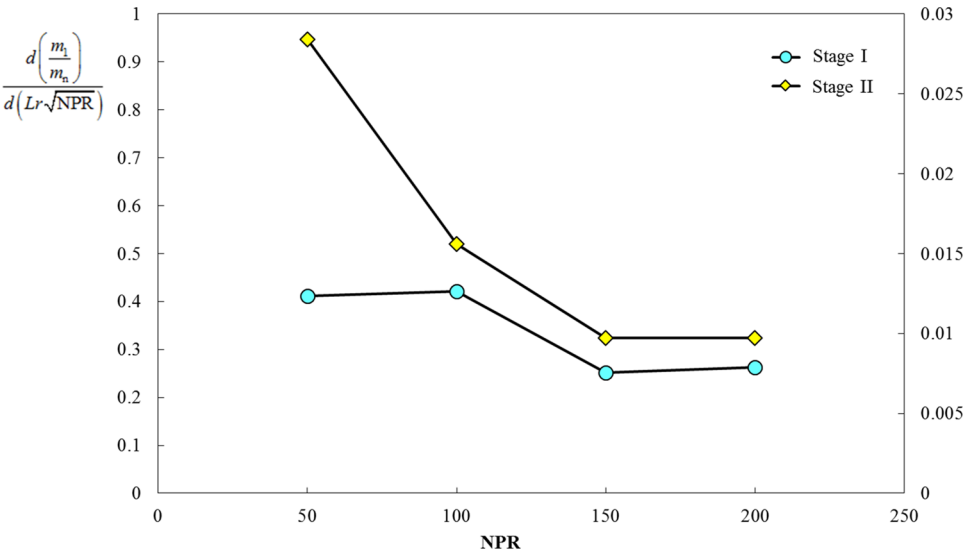

Figure 18. Effect of injection pressure on entrainment rate.

The methane gas jet mass flow rate gradually increases along the jet direction. The entrainment process of the high-pressure methane gas jet has a two-zone feature. In zone I, near field (Lr < 10), the methane jet mass flow rate linearly increases with the increase in Lr and then reaches the maximum. Furthermore, in the nozzle exit field (Lr < 1), no entrainment takes place and the mass flow rate is conserved. In zone II, far field ($Lr \geq 10$), the jet mass flow rate reaches the maximum and the entrainment becomes saturated with a saturation value larger than the initial one at the nozzle outlet.

The entrainment rate m_1/m_n experiences three stages. The curves coincide with each other at the very beginning (stage I), and then they rise and develop (stage II), but at last, all curves tend to coincide again to a constant and become stable (stage III). The m_1/m_n has a linear feature against Lr $(NPR)^{1/2}$ in stage I and early stage II but not in late stage II and stage III.

The methane injection pressure causes great effects on the mass flow rate and entrainment. As injection pressure increases, the methane jet mass flow rate increases linearly, but the entrainment rate decreases. The gas jet entrainment capacity tends to decrease as the pressure increases. Once the injection pressure increases sufficiently high, the m_1/m_n curves tend to be close together with the same slope. Therefore, for a given nozzle size, it is not useful for increasing gas jet entrainment capacity only by increasing the gas jet pressure.

AUTHOR INFORMATION

Corresponding Authors

Yan Lei − *Department of Automotive Engineering, Beijing University of Technology, 100124 Beijing, China;* orcid.org/0000-0003-1732-2703; Phone: +86 13520178609; Email: leiyan@bjut.edu.cn; Fax: +86 10 67391985

Tao Qiu − *Department of Automotive Engineering, Beijing University of Technology, 100124 Beijing, China;*

https://doi.org/10.1021/acsomega.1c04762
ACS Omega 2022, 7, 381−396

orcid.org/0000-0002-6508-1396; Email: qiutao@bjut.edu.cn

Authors

Kai Chang − *Department of Automotive Engineering, Beijing University of Technology, 100124 Beijing, China*

Xiaofeng Wang − *Department of Automotive Engineering, Beijing University of Technology, 100124 Beijing, China*

Chao Qin − *Department of Automotive Engineering, Beijing University of Technology, 100124 Beijing, China*

Dan Zhou − *Hunan Women's University, 410000 Changsha, Hunan, China*

Complete contact information is available at: https://pubs.acs.org/10.1021/acsomega.1c04762

Notes

The authors declare no competing financial interest.

■ ACKNOWLEDGMENTS

The authors gratefully acknowledge financial support for this work by the State Key Laboratory of Engine Reliability Foundations (skler-201913) and National Engineering Laboratory for Mobile Source Emission Control Technology (NELMS2019A06).

■ NOMENCLATURE

d_{nozzle}	nozzle diameter
E_{gas}	gas jet kinetic energy
k	spring elastic coefficient
m	mass flow rate
m_e	entrainment mass flow rate
m_{water}	water mass
p_b	back pressure
R	conventional gas constant
T_{ch4}	methane temperature
u_2	plate moving velocity
V_{CH4}	methane gas jet volume
w	work
Δx	spring plate displacement
z	real gas compression coefficient
ρ_{ch4}	density of the methane
e	kinetic energy
E_{spring}	spring plate kinetic energy
L_r	relative position ratio
m_1	gas jet mass flow rate
m_n	mass flow rate at nozzle outlet
NPR	nozzle pressure ratio
$p_{injection}$	jet pressure
S	gas jet tip penetration
u_1	gas jet velocity
u_n	jet velocity at nozzle outlet
V_{water}	discharge water volume
x	position along the jet direction
x_0	spring plate initial position
ρ	density
ρ_{water}	water density

■ REFERENCES

(1) Kalam, M. A.; Masjuki, H. H. An experimental investigation of high performance natural gas engine with direct injection. *Energy* **2011**, *36*, 3563−3571.

(2) Pourkhesalian, A. M.; Shamekhi, A. H.; Salimi, F. Alternative fuel and gasoline in an SI engine: A comparative study of performance and emissions characteristics. *Fuel* **2010**, *89*, 1056−1063.

(3) Zhang, Q.; Li, M.; Shao, S. Combustion process and emissions of a heavy-duty engine fueled with directly injected natural gas and pilot diesel. *Appl. Energy* **2015**, *157*, 217−228.

(4) Liu, J.; Yu, R.; Ma, B.; Tang, C. On the second explosion limits of hydrogen, methane, ethane, and propane. *ACS Omega* **2020**, *5*, 19268−19276.

(5) Zhao, J.; Liu, W.; Liu, Y. Experimental investigation on the microscopic characteristics of underexpanded transient hydrogen jets. *Int. J. Hydrogen Energy* **2020**, *45*, 16865−16873.

(6) Hamzehloo, A.; Aleifeirs, P. G. Gas dynamics and flow characteristics of highly turbulent under-expanded hydrogen and methane jets under various nozzle pressure ratios and ambient pressures. *Int. J. Hydrogen Energy* **2016**, *41*, 6544−6566.

(7) Yu, J.; Vuorinen, V.; Hillamo, H.; Sarjovaara, T.; Kaario, O.; Larmi, M. An experimental investigation on the flow structure and mixture formation of low pressure ratio wall-impinging jets by a natural gas injector. *J. Nat. Gas Sci. Eng.* **2012**, *9*, 1−10.

(8) Huang, Z.; Shiga, S.; Ueda, T.; Nakamura, H.; Ishima, H.; Obokata, T.; Tsue, M.; Kono, M. Effect of fuel injection timing relative to ignition timing on natural-gas direct injection combustion. *J. Eng. Gas Turbines Power* **2003**, *125*, 783−790.

(9) Mohamad, T. I.; Geok, H. H.; Abdullah, S.; Ali, Y.; Harrison, M.; Jermy, M. *The Combustion and Performance of a Converted Direct Injection Compressed Natural Gas Engine Using Spark Plug Fuel Injector*, SAE Technical Paper Series, 2010-32-0078, 2010.

(10) Distaso, E.; Amirante, R.; Cassone, E.; De Palma, P.; Sementa, P.; Tamburrano, P.; Vaglieco, B. M. Analysis of the combustion process in a lean-burning turbulent jet ignition engine fueled with methane. *Energy Convers. Manage.* **2020**, *223*, No. 113257.

(11) Sakellarakis, V. D.; Vera-Tudela, W.; Doll, U.; Ebi, D.; Wright, Y. M.; Boulouchos, K. The effect of high-pressure injection variations on the mixing state of underexpanded methane jets. *Int. J. Engine Res.* **2021**, *22*, 2900−2918.

(12) Cheng, K.; Chen, X.; Wang, H. X.; Pan, W. X. Modeling study of shrouding gas effects on a laminar argon plasma jet impinging upon a flat substrate in air surroundings. *Thin Solid Films* **2006**, *506*−*507*, 724−728.

(13) Jiang, P.; Liu, X.; Cao, L.; Wang, Q.; He, Z. Experimental study on the gas jet characteristics of a diesel-piloted direct-injection natural gas engine. *J. Mech. Sci. Technol.* **2021**, *35*, 1279−1288.

(14) Dong, Q.; Cai, Z.; Song, E.; Ma, X.; Yao, C.; Huang, T. Characteristics of high-pressure gas jets for natural gas engine based on shock wave calibration. *Trans. CSICE* **2017**, *35*, 44−52.

(15) Cossali, G. E.; Coghe, A.; Araneo, L. Near field entrainment in an impulsively started turbulent gas jet. *AIAA J.* **2001**, *39*, 1113−1122.

(16) Lei, Y.; Liu, J.; Qiu, T.; Li, Y.; Wang, Y.; Wan, B.; Liu, X. Gas jet flow characteristic of high-pressure methane pulsed injection of single-hole cylindrical nozzle. *Fuel* **2019**, *257*, No. 116081.

(17) Ouellette, P.; Hill, P. G. Turbulent transient gas injections. *J. Fluid Eng.* **2000**, *122*, 743−753.

(18) Wang, H. X.; Chen, X.; Pan, W. X. Modeling study on the entrainment of ambient air into subsonic laminar and turbulent argon plasma jets. *Plasma Chem. Plasma Process* **2007**, *27*, 141−162.

(19) Dong, Q.; Li, Y.; Song, E.; Yao, C.; Fan, L.; Sun, J. The characteristic analysis of high-pressure gas jets for natural gas engine based on shock wave structure. *Energy Convers. Manage.* **2017**, *149*, 26−38.

(20) Deng, J.; Zhong, H.; Gong, X.; Gong, Y.; Li, L. Effect of ambient gas on spray and entrainment characteristics of hydrogen jet. *Trans. CSICE* **2019**, *37*, 72−79.

(21) Abraham, J. Entrainment characteristics of transient gas jets. *Numerical Heat Transfer, Part A* **1996**, *30*, 347−364.

(22) Ricou, F. P.; Spalding, D. B. Measurements of entrainment by axisymmetrical turbulent jets. *J. Fluid Mech.* **1961**, *11*, 21−32.

(23) Wang, H. X.; Wei, F. Z.; Meng, X.; Chen, X.; Han, D. S.; Pan, W. X. Direct measurement of the gas entrainment into a turbulent thermal plasma jet. *Plasma Chem. Plasma Process* **2011**, *31*, 127−138.
(24) Azad, M.; Quinn, W. R.; Groulx, D. In *Mean Streamwise Centreline Velocity Decay and Entrainment in Triangular And Circular Jets*, 41st AIAA Fluid Dynamics Conference and Exhibit, AIAA: Honolulu, Hawaii, 2011; pp 2011−3087.
(25) Wang, C.; Liu, F.; Wu, W. Experimental study of the impinging jet diffusion and entrainment for high-pressure injected methane. *Trans. CSICE* **2012**, *30*, 423−428.
(26) Wang, X.; Ye, L.; Liu, Y.; Ma, J. Experiment on entrainment movement of non-isothermal cold jet of circular nozzle based on tracer gas concentration. *J. Water Resour. Water Eng.* **2014**, *21*, 37−45.
(27) Tomita, E.; Hamamoto, Y.; Tsutsumi, H.; Takasaki, S. Ambient gas entrainment into a transient gas jet (Visualization of surrounding air motion and estimation of entrainment amount by path line method. *JSME Int. J., Series B* **1996**, *39*, 546−553.
(28) Karra, P.; Rogers, T.; Lappas, P. *Air Entrainment in Gaseous Fuel Jets Using Particle Image Velocimetry and High Speed Schlieren Photography in A Constant*, SAE [Technical Paper], 2015, 2015-01-0938.
(29) Bruneaux, G.; Causse, M.; Omrane, A. Air entrainment in diesel-like gas jet by simultaneous flow velocity and fuel concentration measurements, comparison of free and wall impinging jet configurations. *SAE Int. J. Engines* **2011**, *5*, 76−93.
(30) Owston, R.; Magi, V.; Abraham, J. *Fuel-air Mixing Characteristics of DI Hydrogen Jets*, SAE [Technical Paper], 2008, 2008-01-1041.

https://doi.org/10.1021/acsomega.1c04762
ACS Omega 2022, 7, 381−396